Title	Quantitative visualization of stable isotope-labeled chromosome using isotope nanoscope
Author(s)	,
Citation	. ( ) 14366
Issue Date	2021-03-25
DOI	10.14943/doctoral.k14366
Doc URL	http://hdl.handle.net/2115/81966
Type	theses (doctoral)
File Information	Kosuke_Nagata.pdf

Instructions for use

Quantitative visualization of stable isotope-labeled chromosome using isotope nanoscope

（同位体ナノスコープによる安定同位体標識された染色体の定量的な可視化）

A dissertation submitted for the doctoral degree of science

presented by

Kosuke Nagata

Department of Natural History Sciences

Graduate School of Science

Hokkaido University

March, 2021

Contents

ABSTRACT

Visualization of DNA strands and chromosomes have been used for the studies of DNA replication, resistance for mutagenesis and DNA repairing, and developed by using radio isotopes or analogs to label nucleotides throughout the cell cycles. However, these labels incorporated into DNA strand restrict the analysis of long-term dynamics of chromosomes because of its mutagenesis resulting in the mutations in cells. We applied stable isotopes for the nucleotide labeling to analyze spontaneous functions of chromosome. In this study, the imaging performance of isotope nanoscope and the consistence of the changes of the label amounts in the chromosomes were studied to evaluate the traceability of stable isotope labels. Firstly, the diameters of primary ion beam with aberration correction mode and non-correction mode were compared with the primary ion current to assess the imaging performance of isotope nanoscope. Aberration corrected primary ion beam showed smaller diameter and twice higher current density at a given lateral resolution. As a result, isotope nanoscope with aberration corrected primary ion beam indicated the abilities to produce fine and dense primary ion beam with lower acceleration voltage resulting in higher lateral resolutions and sensitivities and lower sample disruptions compared with conventional imaging mass spectrometers. Then, the chromosomes in human cultured cell labeled by U-^{13}C$_6$-Glucose throughout the cell cycles were visualized by isotope nanoscope. The heterogeneities of carbon isotope abundance were

observed in each chromosome, and they reflected the semi-conservative replication of DNA strands. The distributions of stable isotope labels also suggested dispersive histone-incorporations into the chromatids. This non-mutagenic and subcellular resolution imaging may be useful to analyze natural functions of organelles with in single cells without radio isotope or analog usages.

1. INTRODUCTION

Chromosome is one of organelle composed of mainly DNA and histone inheriting genomic information to daughter cells during cell divisions. In cell biology, to elucidate the biological systems such as DNA replication and repair mechanisms, chromosomes have been visualized by using the incorporation of radioisotopes and chemical tags in the DNA strands (Liu et al., 2015; Taylor et al., 1957). However, these labels incorporated in the DNA strands behave as mutagens damaging DNA and resulting in the cellular mutations.

For the studies of spontaneous functions in the cells through the cell cycles, stable isotopes are suitable to label DNA strands. Stable isotopes are non-radioactive and do not alter the constitutions of labeled molecules. The visualization of the distinctive distributions of the stable isotope labels in a chromosome needs imaging mass spectrometers which have the spatial resolution of nanometer order.

We applied isotope nanoscope (laser ionization mass nanoscope, LIMAS), which was developed to analyze extraterrestrial materials collected by planetary exploration missions, for the visualization of stable isotope-labeled chromosomes (e.g. Bajo et al., 2015). Isotope nanoscope is the time-of-flight mass spectrometer equipping Ga liquid metal ion source and aberration corrector in the primary column for high spatial resolution (Ebata et al., 2012). Since the imaging performance of isotope nanoscope has been evaluated by only secondary electron

(SE) imaging mode, here we study the performance of the ion imaging to analyze the stable isotope labels in the chromosomes.

In the first chapter, we studied the relations between the primary ion current, lateral resolution and aberration correction in the SE and ion imaging modes of isotope nanoscope to evaluate the imaging performance for the chromosome analysis. Then, in the second chapter, we evaluated the traceability of stable isotope labeling with organelle level by identifying the consistency among the differences in label amount induced by DNA replication.

2. Chapter 1 : ION IMAGING PERFORMANCE OF TIME-OF-FLIGHT SECONDARY NEUTRAL MASS SPECTROMETER

2.1. INTRODUCTION

Imaging mass spectrometry is a useful analytical method to determine three-dimensional spatial distribution for trace elements and isotopes in solid samples. This method has been applied widely to various scientific fields including biology. To achieve a high spatial resolution of nanometers, focused ion beam (FIB) by using the liquid metal ion sources (LMIS) have been applied as primary beams (Hill, 1993; Ishitani and Kawanami, 1995; Kruit and Jiang, 1996; Orloff, 1987; Sakaguchi and Sekine, 1998; Wang, 1997). A pioneering work of Levi-setti et al. (Levi-setti et al. 1985) demonstrated that 20 nm lateral resolution can be achieved for imaging mass spectrometry using Ga^+-probe from LMIS. This resolution, which remains one of the best data, is similar to a broadening estimated from an ion spattering theory on a solid surface by ion probe of keV energy (Levi-Setti and Timothy R. Fox, 1980; Sakamoto et al., 2008). However, applications of Ga^+-probe to imaging mass spectrometer have been limited because secondary ion yields are more than two orders of magnitude lower under Ga bombardment compared with other ion sources (Migeon et al. 1995; Van der Heide. 2014).

Recently there have been developments in secondary neutral mass

spectrometry (SNMS) with strong-field tunneling post-ionization (Bajo et al., 2015; Ebata et al., 2012, 2013; Ishihara et al., 2010) (Figure 1). An isotope nanoscope (laser ionization mass nanoscope, LIMAS) ionized sputtered secondary neutrals ~ 100% (except He which yielded ~ 70%) by irradiation of high power femto-second laser (Ebata et al., 2012; Mibuka et al., 2008; Yurimoto et al., 2016). Consequently, a useful yield improves to 0.2% at mass resolution ($M/\Delta M$) of 600000 [full width at half maximum (FWHM)] for Si (Tonotani et al., 2016). This yield is almost comparable to conventional secondary ion mass spectrometer of 0.7% under $M/\Delta M = 500$ (Hervig et al., 2006) and the low secondary ion yield from the Ga primary beam has not caused weakness in SNMS imaging.

Figure 1: Photograph of isotope nanoscope (Laser ionization mass nanoscope, LIMAS).

Because of an intrinsic energy spread (5-10 eV) of the ions extracted from LMIS 20-21(Bell, 1988; Swanson et al., 1979), chromatic aberration of the primary beam optics limits the probe size and current. The chromatic and spherical aberrations can be eliminated by an electrostatic corrector that is suitable for ion beam optics (Weißbäcker, 2001; Weißbäcker and Rose, 1999, 2000, 2001, 2002; Zach, 2006). The aberration corrector was developed and is installed in isotope nanoscope (Bajo et al., 2016; Ebata et al., 2012; Itose et al., 2011). They

demonstrated the potential to improve the spatial resolution of an ion-induced secondary electron (SE) image.

Here we studied the performance of the chromatic and spherical aberration corrector and spatial resolution of ion images of isotope nanoscope.

2.2. INSTRUMENT

We used isotope nanoscope, an SNMS instrument, at Hokkaido University for our measurements. Figure 2 shows a schematic image of isotope nanoscope. isotope nanoscope consists of gallium LMIS, aberration corrector, femtosecond (fs) laser system (Astrella, Coherent, USA) and multi-turn TOF mass spectrometer (MULTUM II). Primary ion beam is irradiated to sample surface to generate sputtered neutral particles. The sputtered particles are ionized by focused fs laser. Post-ionized secondary neutrals are introduced to secondary ion optics and multi-turn cycles of MULTUM II for TOF mass spectrometry. Finally, separated secondary neutrals which were separated according to mass to charge ratio are detected as by micro-channel plate detector. This is known as secondary neutral mass spectrometry (SNMS).
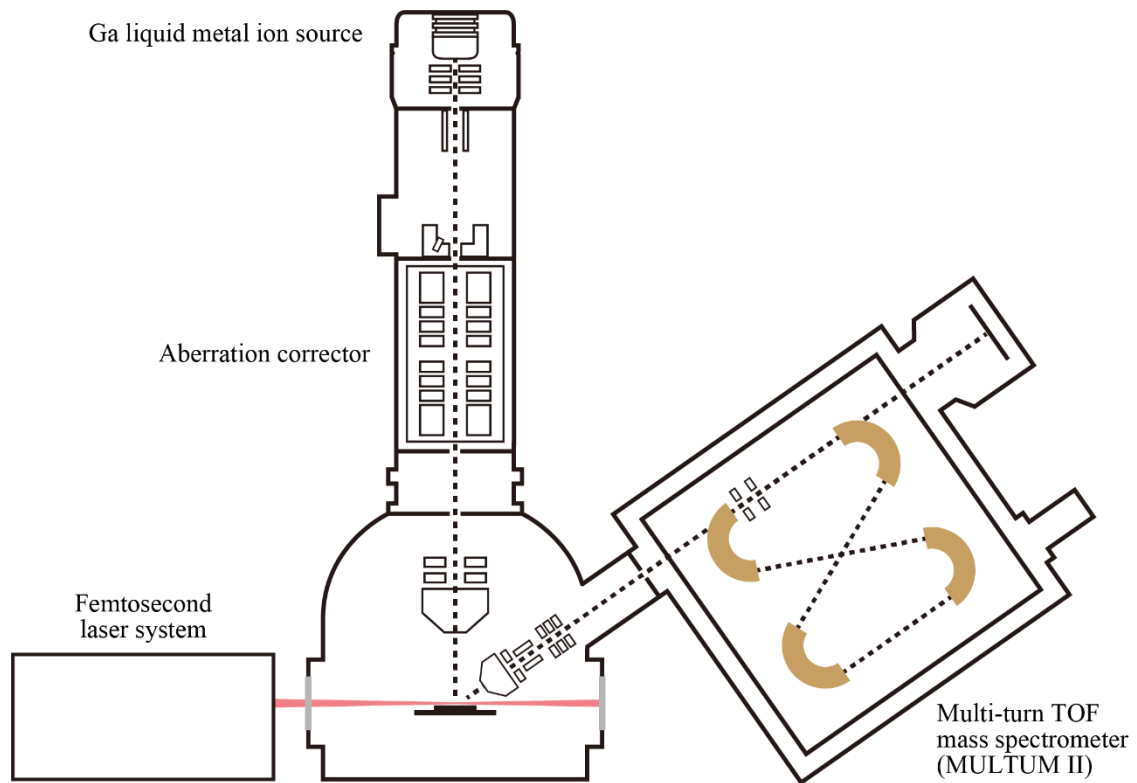
Figure 2: Schematic image of isotope nanoscope (laser ionization mass nanoscope: LIMAS). Dotted line shows the flight path of ions. Red line shows the irradiated laser pathway.

The aberration corrector equipped isotope nanoscope is composed of eight electrostatic dodecapoles (Figure 3). The dodecapoles make dipole, quadrupole, hexapole and octupole fields, which are controlled by graphical user interface on a personal computer. The corrector can correct spherical and chromatic aberrations of primary ion beam by adjusting optical axis and load voltages applying to electrostatic dodecapoles. The combination of Ga LMIS and aberration corrector (gallium focused ion beam system, Ga-FIB) with a primary ion acceleration voltage of 30 kV showed the abilities for elimination of large shallow halo

surrounding deep crater at a primary beam current of 30 nA and focus the probe diameter to 8 nm in size at 3 pA beam current (Bajo et al., 2016).
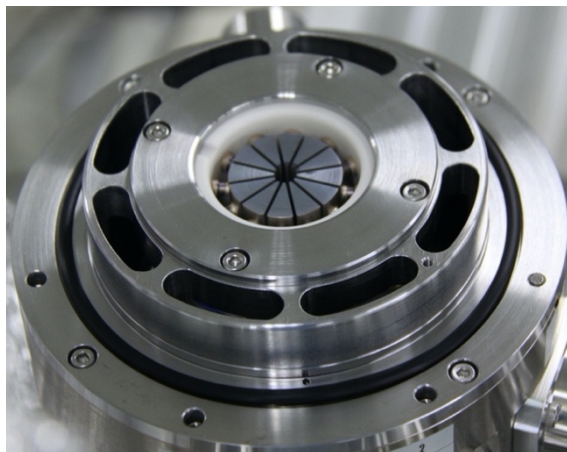

Figure 3: Photograph of an electrostatic dodecapole constructing aberration corrector.

The fs laser beam is focused on the sample surface for tunneling ionization of neutral particles sputtered by Ga-FIB. In the case of Ag^+, ion intensity ionized by 5 nA primary ion beam with laser irradiation which has 40-fs-wide pulses with a pulse energy of 3 mJ was ~1000 times higher than that without laser irradiation (Ebata et al., 2012). The fs laser system installed in isotope nanoscope has been replaced for stronger fields and generates 35-fs-wide pulses with a pulse energy of 6 mJ.

2.3. EXPERIMENTS

We verified the focused ion beam shapes at a given current by time

variations of sputter crater shapes irradiated on Si wafer to study the characterizations of the aberration corrected primary ion beam. Then we obtained SE images and ion images by using focused primary beam with and without aberration corrector. All images were evaluated of lateral resolutions by knife-edge method. To study the specifications of isotope nanoscope imaging, the relationships between the lateral resolution and primary beam current of SE image and ion image were compared.

2.3.1. Sputter crater measurement

The focused beam shapes were verified by measuring of the sputter craters. Continuous primary ion beam focused with and without aberration corrector was irradiated to Si wafer for various sputtering times. The primary current was 3 pA with the acceleration voltage of 20 kV. The sputtering time was managed by control computer for the range of 0.1 to 600 seconds. After sputtering, the diameters of the crater were measured by scanning electron microscope (SEM) (JSM-7000F, JEOL Ltd, Japan) observation.

2.3.2. Knife-edge method

The lateral resolutions of isotope nanoscope images depend on the diameter of primary ion beam, because isotope nanoscope constructs images by primary ion beam scanning. Obtained images were evaluated by using knife-edge method. The method defines the width which correlate to the 16%–84% criterion

of the intensity changes as the lateral resolution. We measured intensity profiles by line scanning across the sharp sample edges (Figure 4). Δx in the Figure 4 indicates the lateral resolution based on 16%–84% criterion. The minimum value among the result of the four line scans was used for the evaluation.
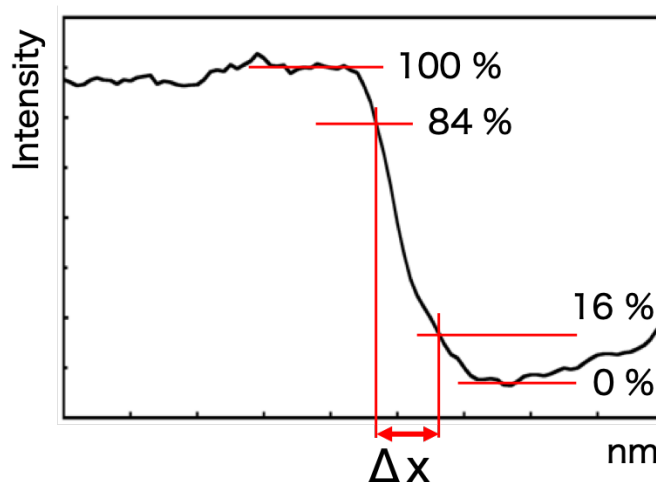

Figure 4: Intensity profile at sharp sample edge and 16%—84% criterion of knife-edge method. The width (Δx) corresponding to the 16—84% of intensity subtraction at the sample edge indicates the lateral resolution.

2.3.3. Analytical conditions

Acceleration voltage of primary ion was 20 kV and the range of primary ion beam current was 1 to 500 pA. Both of aberration correction mode and non-correction mode were used for imaging at each primary ion beam current. Samples were Cu grid masked on Si wafer and Sn particles plated on carbon base (Figure 5). ^{63}Cu was collected from Cu grid. On the other hand, when we analyzed Sn particles, stable isotopes between Sn^{116} to Sn^{120} were accumulated. To obtain ion

images, primary ion beam with pulses to 200 ns width was irradiated and sputtered neutrals were ionized by fs laser beam focused to 50 µm diameter at the laser axis position of 100 µm above sample surface. We accumulated post-ionized ions for 25-200 primary beam pulses at each pixel to collect data. The primary beam was rastered on the sample surface over a pattern of 128 × 128 or 150 × 150 pixels with a step interval depending on the probe diameters used. Analytical conditions are summarized in Table 1.
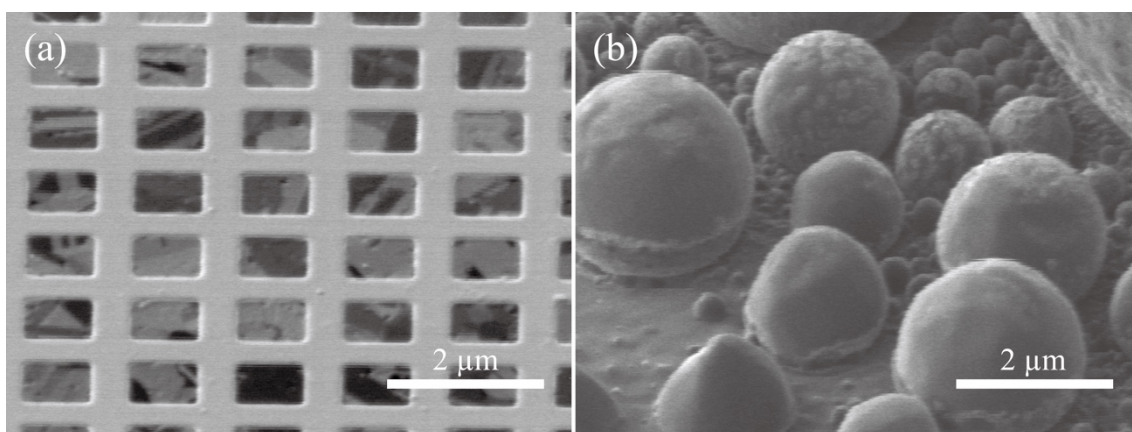

Figure 5: SE image of (a) Cu grid masked on Si wafer and (b) Sn particles plated on carbon base.

Table 1: Analytical conditions of SE and ion imaging

Beam#	Pulse width (ns)	Probe current (pA)	Probe diameter (nm) Corr. ON	Corr. OFF	Pulse number	Dwell time/pixel (µs)	Sputter time/pixel (µs)	Irradiated ions/pixel	Image size (pixel) H	V	Pixel size (nm)	Image size (nm) H	V	Elapsed time/image (s)
SE image														
Beam13	∞	1	11	10	-	65	65	406	1280	960	2.07	2650	1920	80
Beam12	∞	3	12	17	-	65	65	1219	1280	960	2.50	3200	2400	80
Beam11	∞	10	18	23	-	16	16	1000	1280	960	3.34	4270	3203	20
Beam10	∞	26	30	40	-	16	16	2600	1280	960	3.34	4270	3203	20
Beam9	∞	50	36	45	-	16	16	5000	1280	960	5.00	6400	4800	20
Beam8	∞	100	46	78	-	16	16	10000	1280	960	6.66	8530	6398	20
Beam7	∞	300	55	82	-	16	16	30000	1280	960	6.66	8530	6398	20
Beam6	∞	500	106	119	-	16	16	50000	1280	960	10.00	12800	9600	20
ion image														
Beam13	200	1	26	17	200	200000	40	250	128	128	8.33	1066	1066	3277
Beam12	200	3	24	23	100	100000	20	375	128	128	8.33	1066	1066	1638
Beam11	200	10	42	-	100	100000	20	1250	150	150	14.23	2135	2135	2250
Beam11	200	10	-	32	100	100000	20	1250	128	128	15.03	1924	1924	1638
Beam10	200	22	47	-	100	100000	20	2750	128	128	15.03	1924	1924	1638
Beam10	200	22	-	56	100	100000	20	2750	150	150	14.23	2135	2135	2250
Beam9	200	41	83	71	60	60000	12	3075	128	128	22.52	2883	2883	983
Beam6	200	400	143	131	25	25000	5	12500	150	150	42.67	6401	6401	563

2.4. RESULTS

Figures 6 and 7 show the SE images of the sputtering craters on Si wafer formed by primary ion beam irradiation with and without aberration corrector. The successive sputter time expanded the diameter of the craters and formed a deep crater in the center and surrounding halo crater (Figures 6 and 7). The data values of deep and halo craters at given sputter time are shown in Table 2. The diameter variations as a function of the inverse of sputter time demonstrated the distribution of the primary beam intensity along radial directions (Figure 8). The intensity distribution at the deep craters approximated to Gaussian distribution function, which has the standard deviation σ. Beam diameter 2σ is 11.7 nm with aberration correction and 20.2 nm without correction. The intensity profile for aberration correction and non-aberration correction depart from Gaussian distribution at 2% and 5% of peak, respectively.
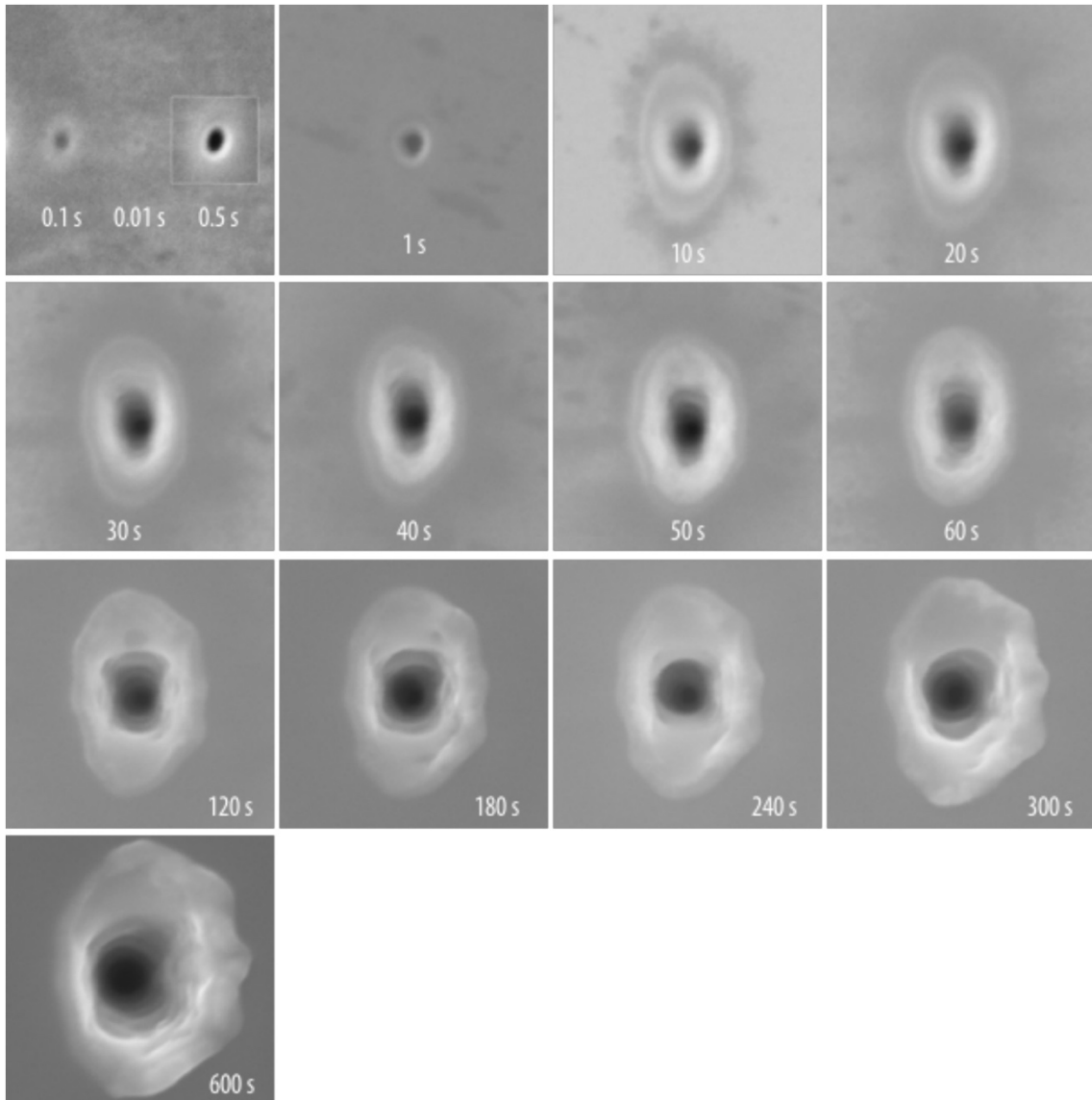
Figure 6: SE images of sputtering craters on Si wafer formed by aberration corrected primary ion beam. Irradiation time is indicated under the craters (0.01—600 s). Deep crater is appeared as the center black hole. Field of view: 700 nm.
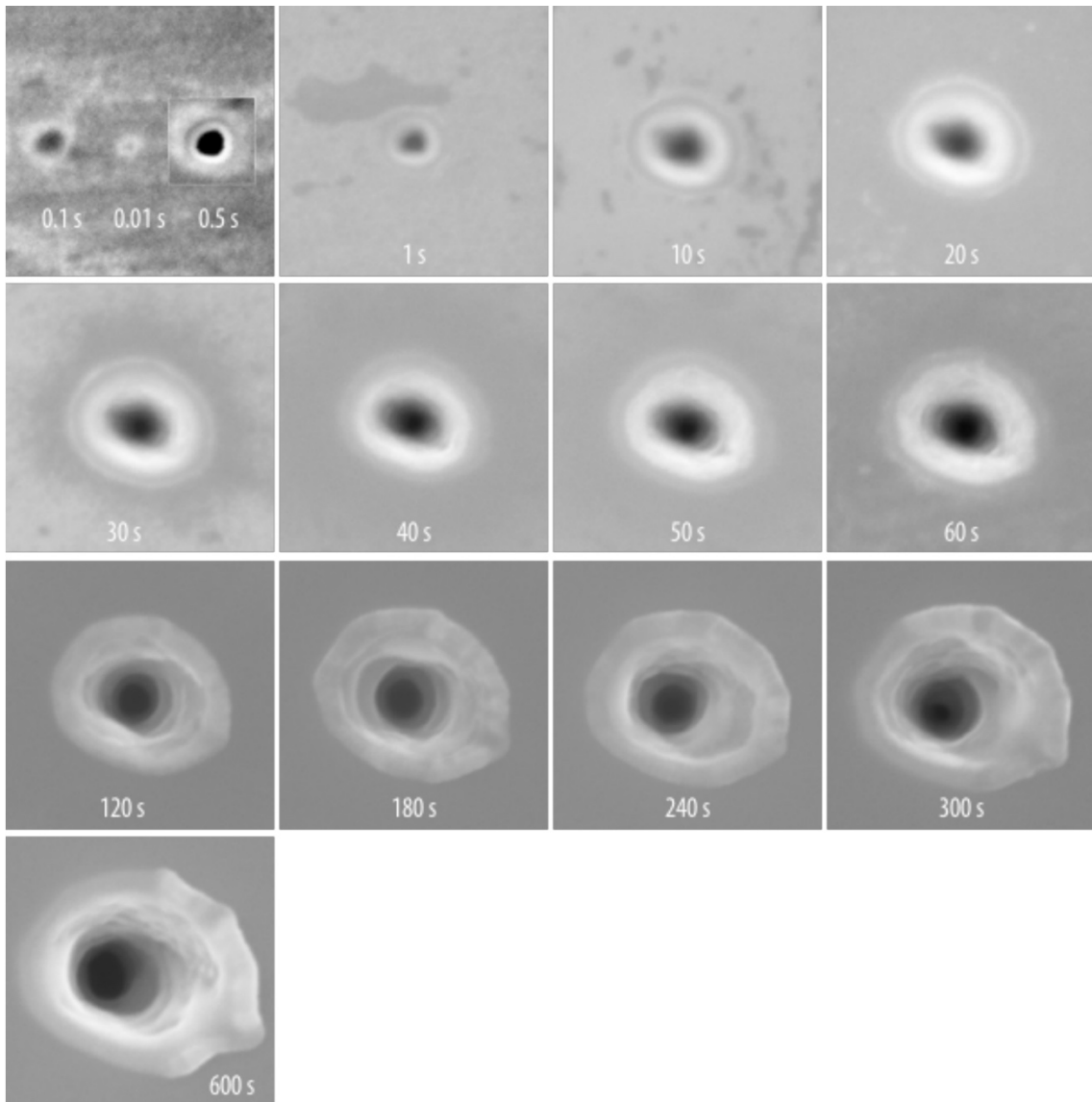
Figure 7: SE images of sputtering craters on Si wafer formed by non-corrected primary ion beam. Irradiation time is indicated under the craters (0.01—600 s). Deep crater is appeared as the center black hole. Field of view: 700 nm.

Table 2: Data values of deep and halo craters

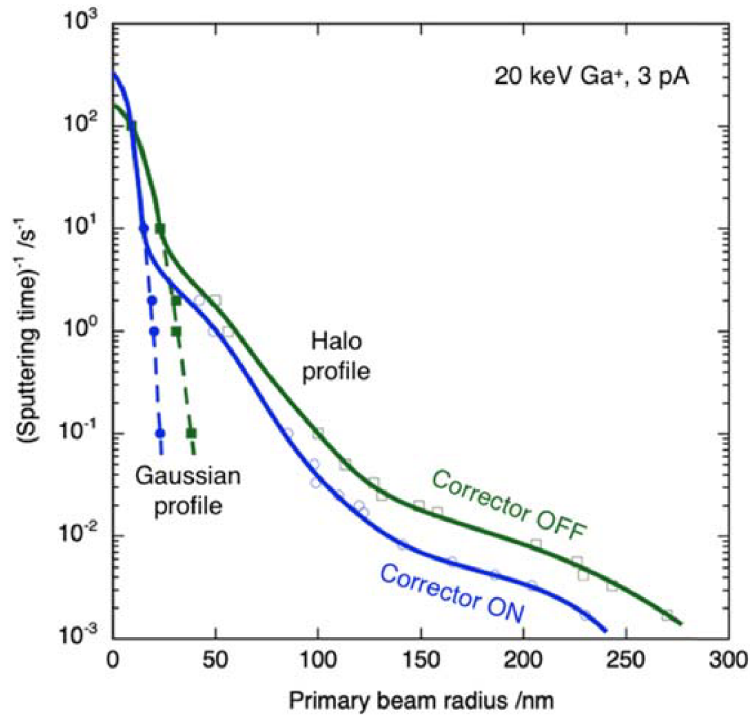| Sputter time (s)	Correction ON		Correction OFF	
	Deep crater diameter (nm)	Halo crater diameter (nm)	Deep crater diameter (nm)	Halo crater diameter (nm)
0.01	19	–	19	–
0.1	30	–	45	–
0.5	38	84	62	99
1	39	98	62	113
10	47	171	75	201
20	–	195	–	225
30	–	199	–	253
40	–	219	–	263
50	–	240	–	298
60	–	244	–	315
120	–	281	–	413
180	–	330	–	452
240	–	371	–	458
300	–	409	–	486
600	–	459	–	540

Figure 8: Relationship between the inverse of sputter time and the primary beam radius. Solid symbol: deep crater, open symbol: halo crater, solid line: radial intensity distribution, dashed line: Gaussian function approximation. Original images of sputtering craters are shown in Figures 6 and 7. The data values are shown in Table 2.

The relationship between primary ion beam current and lateral resolution which obtained by knife-edge method is illustrated and compared with conventional imaging mass spectrometers in Figure 9. The lateral resolutions for all images increased linearly with the decrease of primary beam current. Then the lateral resolution for ion image achieved to over 20 nm with aberration corrected beam of 3 pA. The aberration corrector efficiently improved the lateral resolution determined from SE image. On the other hand, the lateral resolution for ion image was not differed basically between correction mode and non-corrected mode and

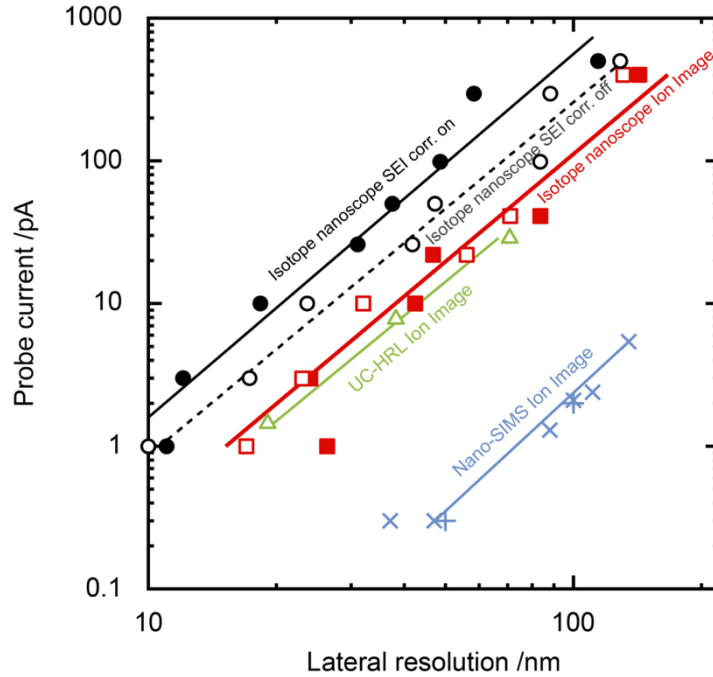always resulted in lower than that for SE image.

Figure 9: Relationship between the primary beam current and the lateral resolution of imaging mass spectrometers. Solid circle: isotope nanoscope SE image under aberration correction mode by 20 keV Ga^+ primary ion beam, open circle: isotope nanoscope SE image under non-correction mode by 20 keV Ga^+ primary ion beam, solid square: isotope nanoscope ion image under aberration correction mode by 20 keV Ga^+ primary ion beam, open square: isotope nanoscope ion image under non-correction mode by 20 keV Ga^+ primary ion beam, open triangle: UC-HRL ion image by 40 keV Ga^+ primary ion beam, cross: NanoSIMS ion image by 20 keV O^- primary ion beam, plus: NanoSIMS ion image by 20 keV Cs^+ primary ion beam.

2.5. DISCUSSIONS

Beam diameter 2σ which calculated from beam craters demonstrated that the aberration corrector decreased the diameter of the primary ion beam to 1/1.7. It is close to the theoretical estimation (1/2–1/3). The characteristics of the beam intensity profile for non-correction are similar to that for correction, but the halo percentage in the beam intensity profile is larger (Figure 8). Therefore, the aberration corrector reduces the ion optical aberration and consequently increases the beam densities. The lateral resolutions of SE image obtained by 3 pA primary ion beam, which is the same condition with the crater shape measurement, were calculated by knife-edge method. The values are 12 nm in correction mode and 17 nm in non-correction mode, and equivalent with the ion beam diameters defined by the crater shape method. Therefore, the diameter of primary ion beam can be determined by the lateral resolution of SE image. The diameter of primary ion beam at a given primary current is approximately 1.4 times smaller in aberration correction mode than non-correction mode over the primary current ranges 1 pA–1 nA and down to 10 nm at 1 pA (Figure 9). In other words, the primary current at a given beam diameter is about two times larger with aberration correction than without aberration correction. The fine and dense primary ion beam with aberration correction may be useful for mass analysis of small samples with size of several 10 nm. Lateral resolutions of the ion imaging, however, are lower than the diameter of the primary ion beam at a given primary current and are basically

the same either in aberration correction mode or in non-correction mode (Figure 9).

The insignificance of aberration correction in ion imaging and the difference of the lateral resolution between SE image and ion image can be attributed to the image acquisition process. The small mechanical vibration of the sample stage is observed as the jitters of approximately 20 nm at the edge of Sn particles of the SE image (Figure 10a and b). The dwell time at a pixel for ion imaging (25–200 ms) is much longer than those for the SE imaging (16–65 μs). In the ion images, the vibration was averaged and incorporated into several pixels, and consequently the jitters disappeared (Figure 10c and d). Therefore, the lateral resolution determined from ion image is limited to approximately 20 nm under both with and without aberration correction (Figure 9). However, the jitters are not only reason for the differences in lateral resolution between SE image and ion image, because they increase from 10 to 40 nm when primary currents also increase (Figure 9). Because irradiated ion numbers at a pixel are larger for the SE images than for ion images under the same primary current, the differences are not caused by modification of sample surface by sputtering (Table 1). Because the dwell time at a pixel of ion images becomes shorter with increasing primary current, the differences are not caused by sample stage drift or primary beam drift. The SE images determined the diameter of the primary ion beam, however the lateral resolutions of ion images were approximately half the size of the beam diameters. Further study is necessary to clarify reasons for the differences.
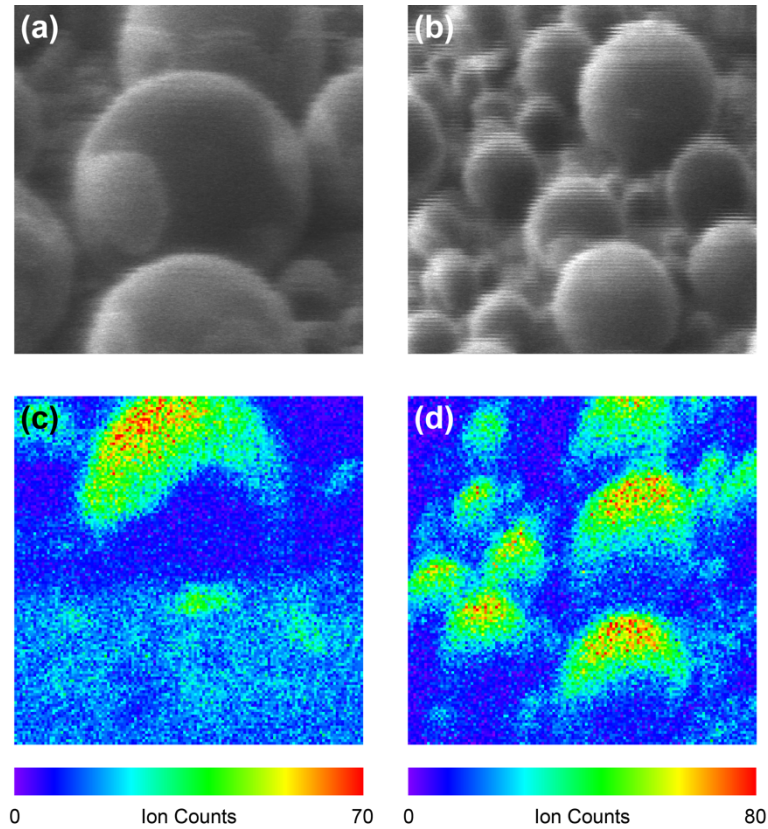
Figure 10: SE images and ion images of Sn particles on the carbon substrate obtained using aberration correction or non-correction mode. Ga^+ beam with primary ion current of 3 pA and 20 kV of primary acceleration voltage was used. FOV (a) SE image under aberration correction mode. (b) SE image under non-correction mode. (c) Ion image under aberration correction mode for combined Sn isotopes of $^{116}Sn^+$, $^{118}Sn^+$ and $^{120}Sn^+$. (d) Ion image under non-correction mode for combined Sn isotopes of $^{116}Sn^+$, $^{118}Sn^+$ and $^{120}Sn^+$. Field of view: 1100 nm.

The Cameca NanoSIMS is a commercial SIMS designed to obtain high lateral resolution images in nanometer scale (Malherbe et al., 2016). Primary beam current at a given lateral resolution is fifty to one hundred times higher in the isotope nanoscope image than in the NanoSIMS image which used radio frequency O^- plasma source and thermal ionization Cs^+ source (Figure 9). The UC-HRL

SIMS is one of the instrument which can obtain the highest lateral resolution SIMS image (Levi-setti et al. 1985). The lateral resolution of the UC-HRL SIMS image is comparable to that of the isotope nanoscope image at a given primary beam current although the acceleration voltage was set to 40 kV for the UC-HRL SIMS and 20 kV for the isotope nanoscope. Thus, aberration-corrected FIB provides the primary ion beam with higher current density and lower acceleration voltage, which achieves smaller diameter and higher lateral resolution. The smallest primary beam diameter produced with the aberration-corrected FIB was 10 nm with a current of 1 pA of $^{69}Ga^{+}$ primary ions at an impact energy of 20 keV.

2.6. SUMMARY

Aberration corrector to reduce the chromatic and spherical aberrations which appear in primary ion beam was developed and installed in a Ga-FIB of isotope nanoscope. At a given primary ion current over ranges from 1 to 500 pA, Ga^+ beam adjusted with aberration corrector was focused ~1.5 times smaller than without aberration corrector. The primary ion current at a given probe diameter in correction mode was two times larger than that in non-correction mode. Thus, the aberration corrector performed efficiently to produce fine and dense primary ion beam and achieved the probe diameter down to 10 nm at 1 pA with the acceleration voltage of 20 kV. The lateral resolution of ion image increased with the reduction of primary ion current and achieved down to 20 nm at 1 pA with the acceleration voltage of 20kV.

3. CHAPTER 2: VISUALIZATION OF STABLE ISOTOPE-LABELED CHROMOSOMES USING ISOTOPE NANOSCOPE

3.1. INTRODUCTION

As deoxyribonucleic acid (DNA) strands are carriers of genetic information, each DNA strand must be replicated in the parent cell before cell division. DNA replication accords to a process referred to as semi-conservative replication, which synthesizes two new strands using the unzipped pre-existing strands as templates. The semi-conservative DNA replication was predicted by Watson and Crick (Watson and Crick, 1953) and demonstrated experimentally by Meselson and Stahl (Meselson and Stahl, 1958). They showed displacement of labeled DNA fractions following cell divisions by stable isotope labeling of 15N and density gradient centrifugation using *Escherichia coli*. However, their experiment could not address the replicative characteristics of individual chromosomes, which could be greatly diverse even within a cell (Dileep and Gilbert, 2018; Takahashi et al., 2019).

Taylor et al. (Taylor et al., 1957) first succeeded in visualizing semi-conservative replication of a single chromosome using tritium-labeled thymidine (^{3}H-dT). Visualization of chromosome replication in a powerful technique to detect mitotically active cells, trace the progression of cell divisions or observe

massive DNA repairs, such as homologous recombination. Therefore, many alternative methods using nucleotide analogs such as bromodeoxyuridine (BrdU) have been developed for the visualization (Gratzner et al., 1975; Latt, 1973; Levi-Setti and Le Beau, 1992; Perry and Wolff, 1974; Pinkel et al., 1985). However, a relatively short lifetime of radioisotopes or frequent mutagenesis caused by nucleotide analogs and fluorescent labels largely restrict the utility of the techniques in investigating the long-term dynamics of chromosome segregations in multiple rounds of cell cycles (Solary et al., 1992; Taupin, 2007).

Stable isotope labels are available for labeling nucleic acids instead of the use of radioisotopes and thymidine analogs. Stable isotopes such as ^{13}C, ^{15}N and ^{18}O have been used as markers without disturbing biological metabolism and secondary ion mass spectrometry (SIMS) has been used for the visualization (Hamasaki et al., 2013; Kuga et al., 2014; Lechene et al., 2006; Steinhauser et al., 2012). However, stable isotope imaging has been limited to tracing cellular-level metabolism (Steinhauser et al., 2012). Indeed, stable isotope imaging has not visualized DNA replication of single chromosomes. Visualization of spatiotemporal distribution of stable isotopes within organelles such as chromosome and changes in isotope labeling through cell cycles are challenges to the next stage.

In this study, we have visualized the distributions of stable isotope labels incorporated into chromosomes of a human cultured cell. Aberration corrected primary ion beam of 400 pA with the lateral resolution of about 100 nm, which

was determined in chapter. 1, was used for ion imaging. Moreover, we quantitatively specified the dynamics of the segregation of the labeled chromosomes throughout successive cell divisions using stable isotope imaging. This analog label-free imaging also enables tracing of protein recycling through cell cycles, paving the way for analyzing diverse characteristics within individual organelles. Finally, we introduce the analysis of sister chromatid exchange frequency as an application of stable isotope labeling method.

3.2. EXPERIMENTS

We used ^{13}C for stable isotope label and introduced into cultured cells as U-^{13}C$_6$-Glucose. Cultured cells were previously incubated with stable isotope labeled medium to make ^{13}C-enriched cell, which has ^{13}C-enriched double strand (ds)DNA throughout the chromosomes (cycle-0). Then the labeled cells were transferred to the medium which has natural carbon isotope abundance [^{13}C/(^{13}C + ^{13}C) = C$_r$] and incubated continuously. ^{13}C labels in the DNA reduce according to the semi-conservative replication though they also distribute homogeneously in the chromosomes in the cell incubated for one cell cycle with the replaced medium (cycle-1). Consequently, the chromosomes in the twice divided cells after the medium replacement are expected to have ^{13}C-rich chromatid and ^{13}C-poor chromatid (cycle-2) (Figure 11). Glucose and its digestives are used for energy source of biological reactions and for precursors of biomolecules (amino acid, lipid,

27

nucleotide, etc). Because stable isotope labels are incorporated into not only the DNA but also the proteins, it disables to determine the characteristics of the ^{13}C distributions in the DNA. Therefore, we simultaneously used bromodeoxyuridine (BrdU), which is one of the thymidine analogs, to identify the relationship of the distributions between ^{13}C label and DNA. Because BrdU is incorporated into newly synthesized DNA, the cycle 2 cells have Br-rich chromatid and Br-poor chromatid and all the Br-rich chromatids distribute complementarily with the ^{13}C-rich chromatids in single chromosome (Figure 11).
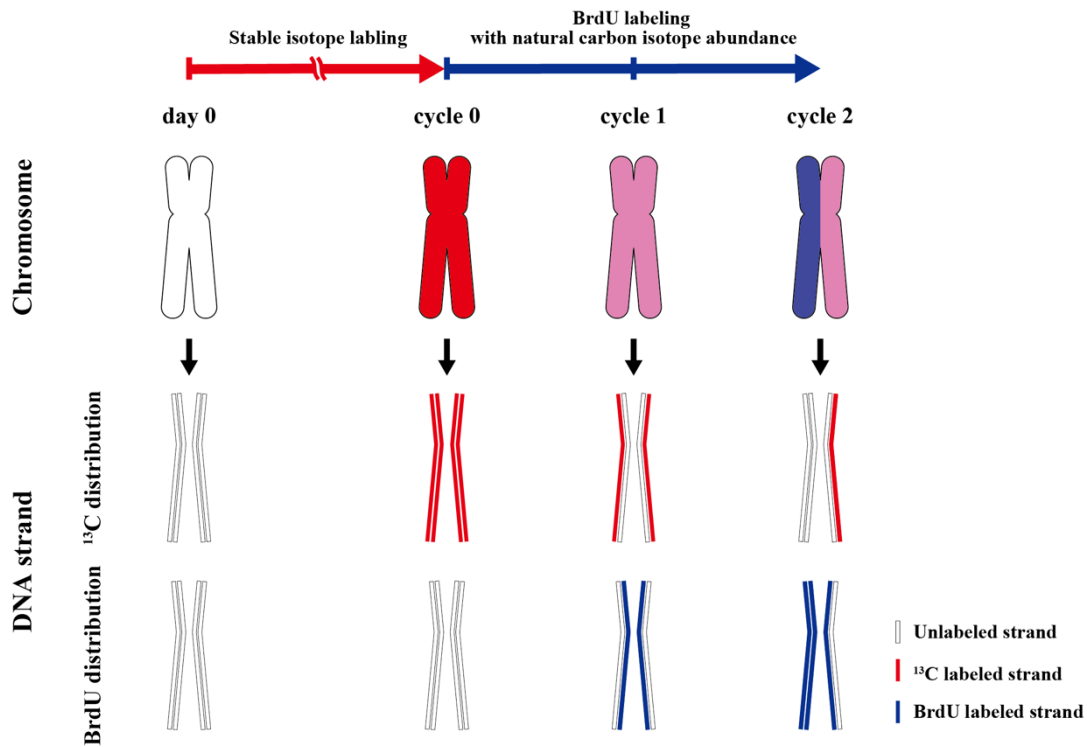
Figure 11: Schematic image of ^{13}C and BrdU labeled chromosome and labeling state of DNA strands composing the chromosome. At day 0, chromosome and DNA strands contain no labels. After stable isotope labeling (cycle-0), chromosome and DNA strands are enriched by administrated ^{13}C. After first cell cycle in exchanged medium (cycle-1), newly DNA strands contain BrdU and little ^{13}C. Therefore, cycle-1 chromosome shows uniform distributions of ^{13}C and Br ions. After second cell cycle (cycle-2), DNA strands synthesized from exchanged medium compose either ^{13}C-poor but Br-rich chromatid. Consequently, cycle-2 chromosome shows complement distribution of ^{13}C-rich chromatid and Br-rich chromatid.

3.2.1. Labeling protocol

HeLa cells were cultured in 2 mL of culture medium in tissue culture dishes with a diameter of 35 mm in the dark under a humidified 5% CO_2/95% atmosphere at 37 ˚C. Cells were maintained in Dulbecco's modified Eagle's

medium (DMEM) (Sigma) supplemented with 10% FBS (Sigma) and penicillin (100 unit/mL)–streptomycin (100 µg/mL) (Wako) by seeding 2.5×10^4 cells per dish. The maintained cells were washed with PBS (1.0 mL) and incubated with glucose free DMEM (Wako) supplemented with U-^{13}C$_6$-Glucose (1 mg/mL) (Cambridge Isotope Laboratories, Inc.) (2.0 mL), 10% FBS (Sigma) and penicillin (100 unit/mL)–streptomycin (100 µg/mL) (Wako) for ^{13}C isotope labeling. Cells were maintained for 1 week with 3 passages. At third passage, the cells were transferred to two dishes. After stable isotope labeling, the cells in the one dish were collected for chromosome spread preparation. The cells in the other dish were washed with PBS (1.0 mL) and incubated with Glucose (1 mg/mL) (natural carbon isotope abundance: 0.011)-containing DMEM (Sigma) (2.0 mL) supplemented with BrdU (15 µM) (Sigma), 10% FBS (Sigma) and penicillin (100 unit/mL)–streptomycin (100 µg/mL) (Wako). After 32 h incubation with BrdU labeled medium, the cells were collected for chromosome spread preparation. Whole of the labeling flow is illustrated in Figure 12.
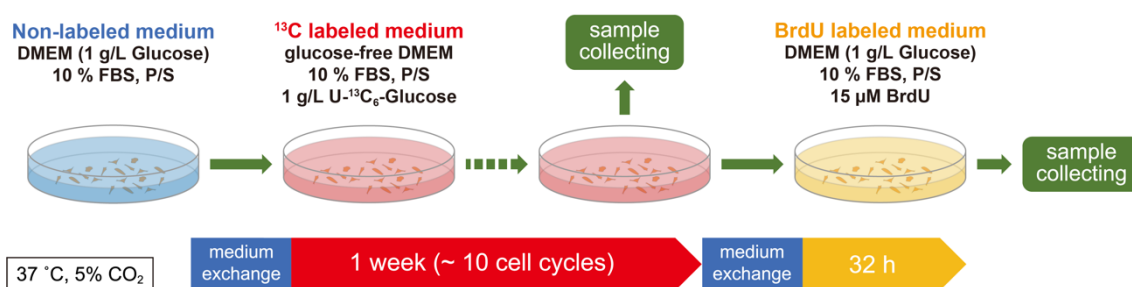
Figure 12: Schematic protocol of U-$^{13}C_6$-Glucose and BrdU labeling. HeLa cells were cultured with stable isotope labeled DMEM containing 1 mg/mL U-$^{13}C_6$-Glucose for 1 week. After stable isotope labeling, a part of cells was processed to sample preparation. The rest were cultured with BrdU labeled DMEM which has natural carbon isotope abundance. Then, cells were incubated for 32 hours to process to sample preparation. At every medium replacement, cells were washed with PBS.

3.2.2. Sample preparation

The cells were treated with colcemid (50 ng/mL) (Nacalai Tesque Inc.) for 2 h, resulting in the arrest of the cell cycle in mitosis. Then the cells were harvested and washed with PBS. The cells were treated with hypotonic KCl (75 mM, 8 min) followed by 5 changes of fixative (absolute methanol : acetic acid, 3 : 1) (Levi-Setti and Le Beau, 1992). Droplets of cell suspensions were dropped on the Si wafer (5×5 mm^2) and air dried. The location of chromosome spreads was observed by using scanning electron microscope (JEOL JSM-7000F). Primary beam current of 2 nA with acceleration voltage of 5 keV was used to acquire SE image of whole area of Si wafer (Figure 13). In Figure 13, individual cells were visualized as black spots. Many cells were in mitosis showing chromosome spread. Chromosome spread was observed by a SE image using isotope nanoscope (Ebata

et al., 2012) (Figure 14). Ga-FIB with primary current 3 pA and acceleration voltage of 20 kV was used to obtain the ion-induced SE image. The 56 chromosomes enclosed by cell components from a chromosome spread were observed. The analyzed spread cell area was easily distinguished from other spread areas apart from it.
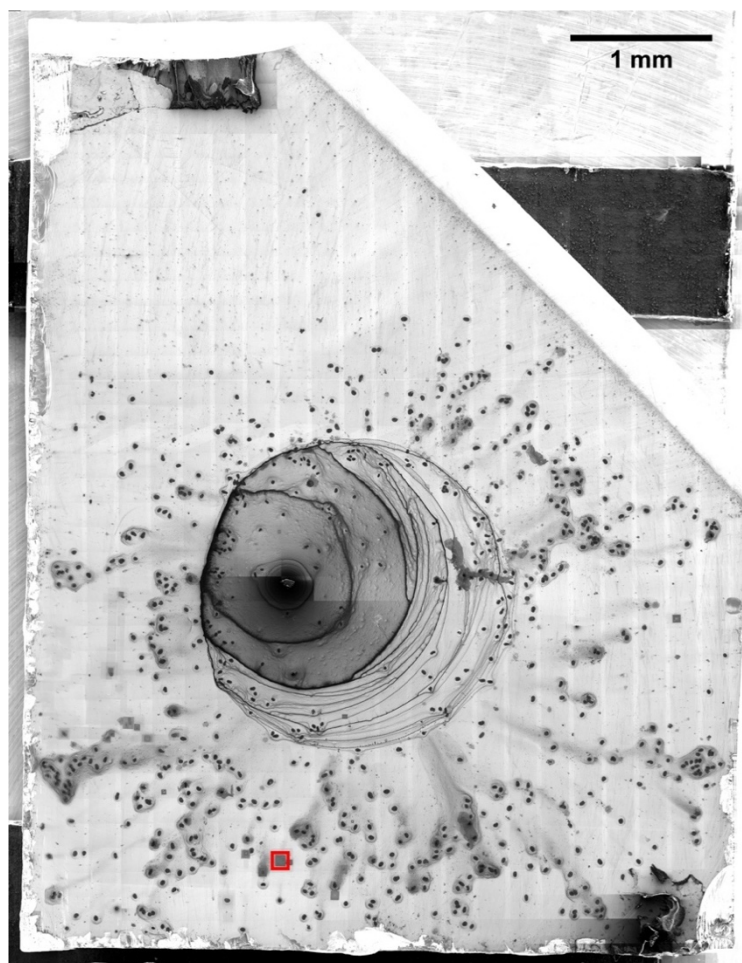

Figure 13: Secondary electron image of chromosome spreads dropped on Si wafer substrate. A chromosome spread marked by red square is shown in Figure 14.
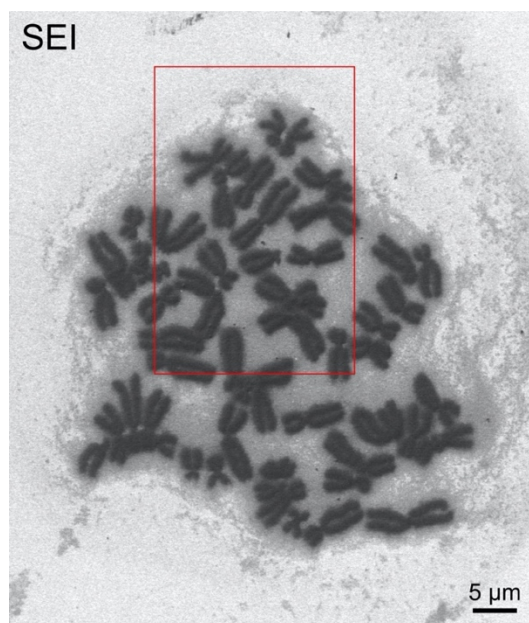
Figure 14: Secondary electron image of a chromosome spread of one HeLa cell. The interspace between each chromosome is filled with cell components. Red square indicates scanning area to obtain an ion image shown in Figures 17, 18b and 20.

3.2.3. Analytical conditions

Isotope distribution on the chromosome spread was observed by isotope nanoscope. Ga-FIB with aberration correction mode focused ion beam to a diameter of 100 nm at a current of 400 pA with acceleration voltage of 20 kV (Nagata et al., 2019). The primary ion beam was scanned on the sample surface for 300 × 300 pixels, resulting in ion image acquisition. The scanned area corresponded to an area of $19.2 \times 33.7 \ \mu m^2$, of which pixel size was $64 \times 112 \ nm^2$, because the incident angle of the primary beam on the sample was set to 35° from the sample surface. Post-ionized ions were accumulated for 500 primary beam pulses at each pixel to collect data. Before data collection, the surface of

chromosome spread was presputtered by the irradiation of 4×10^7 ions/μm^2 using the same focused beam as ion imaging until Si wafer substrate appears (Figure 15).
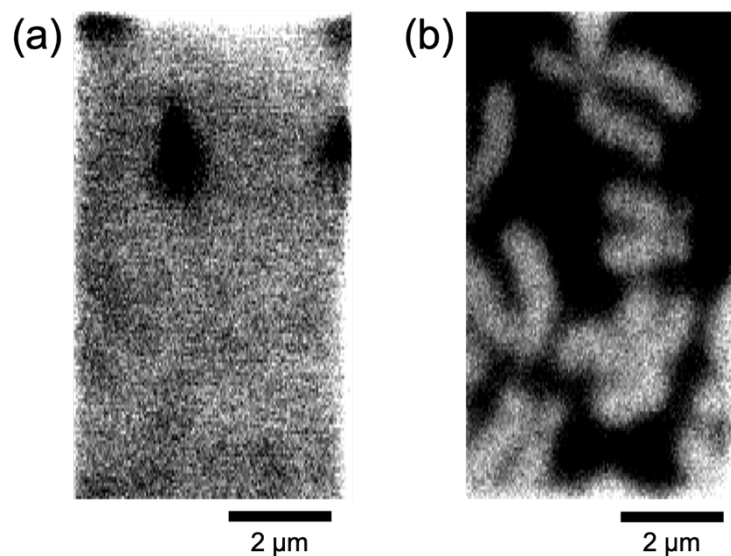

Figure 15: ^{12}C ion image of chromosomes before (a) and after (b) presputtering. Before presputtering, chromosomes were covered by cell components. After presputtering, cell components were sputtered out and chromosomes were appeared.

Post-ionized ions of ^{12}C$^+$, ^{13}C$^+$, ^{28}Si^{2+}, ^{79}Br^{2+} and ^{81}Br^{2+} sputtered from sample surface were observed. The post-ionized ions which mass to charge ratios are 12-14 and 39-43 were introduced to MULTUM II. The other ions were eliminated by using ion gate to limit the peak number, resulting in reduction of the peak overlapping and easy peak assignment. The ^{13}C$^+$ peak (isotopic mass: 13.0034) from chromosomes was contributed by ^{12}CH$^+$ peak (isotopic mass: 13.0078) as the interference. ^{13}C$^+$ and ^{12}CH$^+$ flighted 20 cycles in MULTUM II and separated at the mass resolving power of 6800 (FWHM) (Figure 16). In this analytical condition. No interference peaks were detected for the other ions.
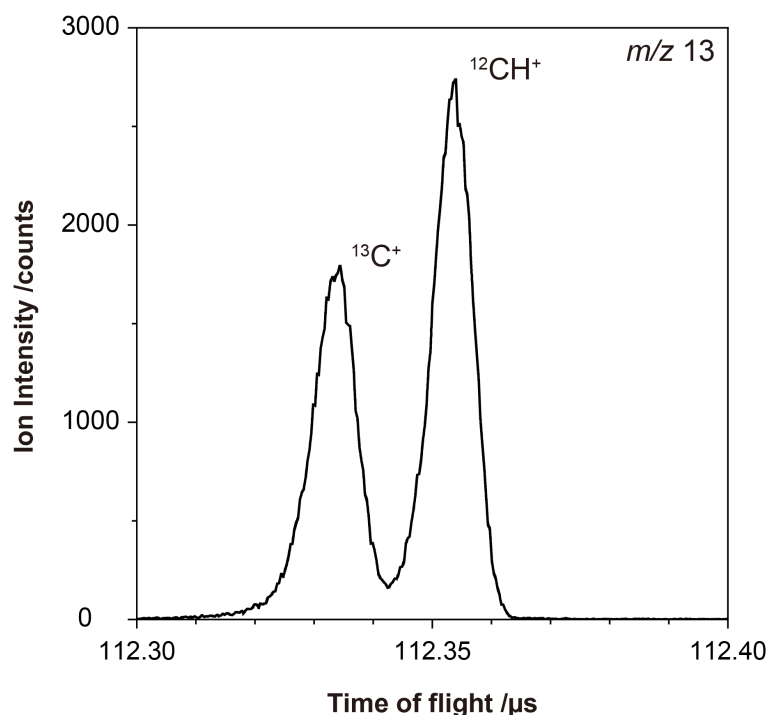
Figure 16: Mass spectrum by time of flight between 112.3–112.4 µs corresponding to *m/z* 13.

Total counts of $^{79}Br^{2+}$ + $^{81}Br^{2+}$ isotopes were used for Br ion images. ^{13}C and Br counts were normalized by total carbon counts (^{12}C + ^{13}C) to correct small instrumental fluctuation changes of ion intensities during measurements. Smoothing filter for 3 × 3 pixels was applied to isotope images in order to reduce statistical noises. Signals outside chromosomes were masked by $^{28}Si^{2+}$ intensities which are generated from the Si substrate (Figure 17). Ion images of the chromosome spread were shown in Figures 18 and 19.
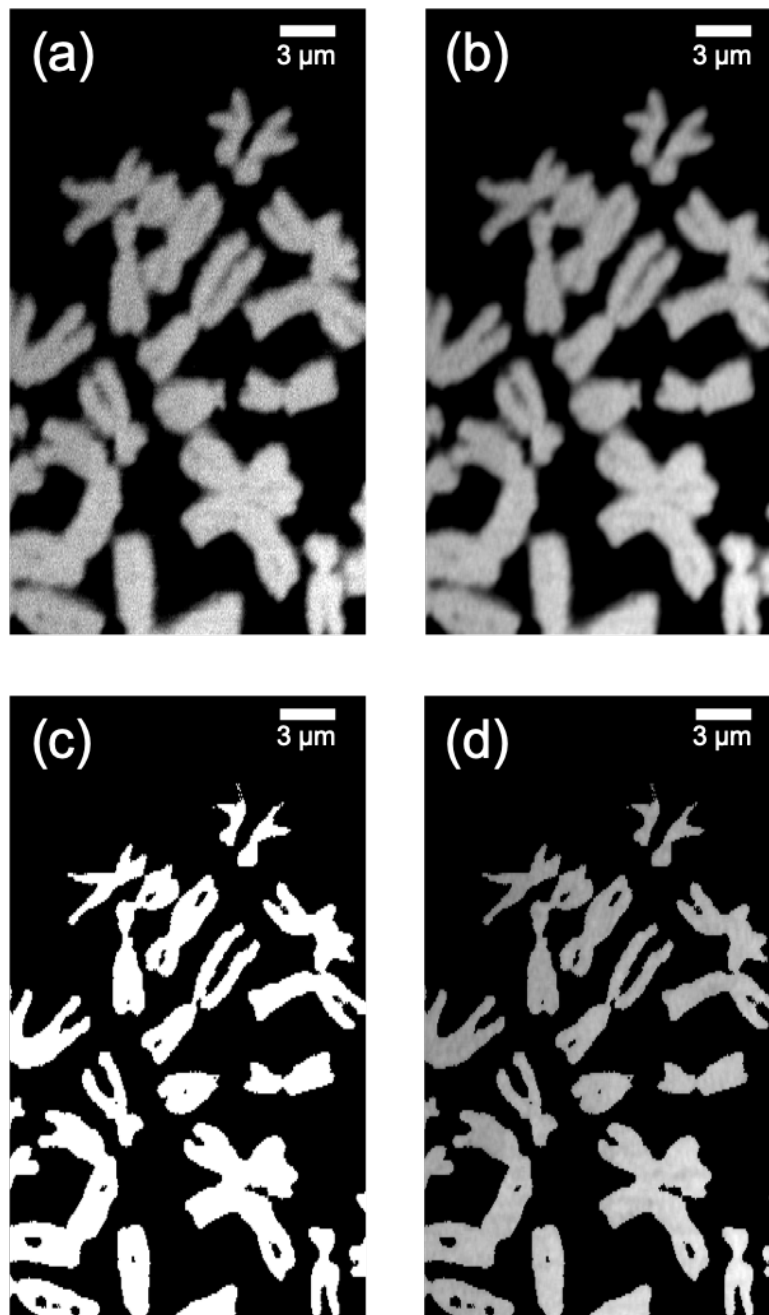
Figure 17: Carbon (^{12}C + ^{13}C) images of an area of red square of Figure 14. (a) Raw image. (b) 3 × 3 smoothing image. (c) Mask of chromosomes made by ^{28}Si image. (d) 3 × 3 smoothing image applied the mask of chromosomes.

3.2.4. Histogram and curve fitting

Histograms obtained from carbon isotope abundance (^{13}C / ^{12}C + ^{13}C) images of chromosomes (Figures 19 and 20b) are shown in Figure 21a. Peak A (isotope abundance: 0.155–0.305) is constructed from the isotope abundance of Figure 19. Peak B (0.030–0.130) corresponds with the isotope abundance of Figure 20b. Red line of Figure 21 indicates a Gaussian curve fitted to Peak A by using least-squares method. There are two peaks (Peak B_1 and Peak B_2) in Peak B. The left peak corresponds to the region of the ^{13}C-poor chromatid and the right peak to the ^{13}C-rich chromatid. The value of the valley between two peaks (a yellow bin of Figure 18a: 0.08–0.085) mostly corresponds to the region of the sister chromatid cohesion (yellow pixels of Figure 18b). Thus, Gaussian curves were fitted to peak B without the valley of the two peaks by using least-squares method (Figure 21a). Two Gaussian curves were fitted to Peak B1 (0.085–0.150) and Peak B2 (0–0.080) (green and blue lines of Figure 21a, respectively). The composite of two Gaussian curves provides a good approximation of Peak B (dashed line of Figure 21a).
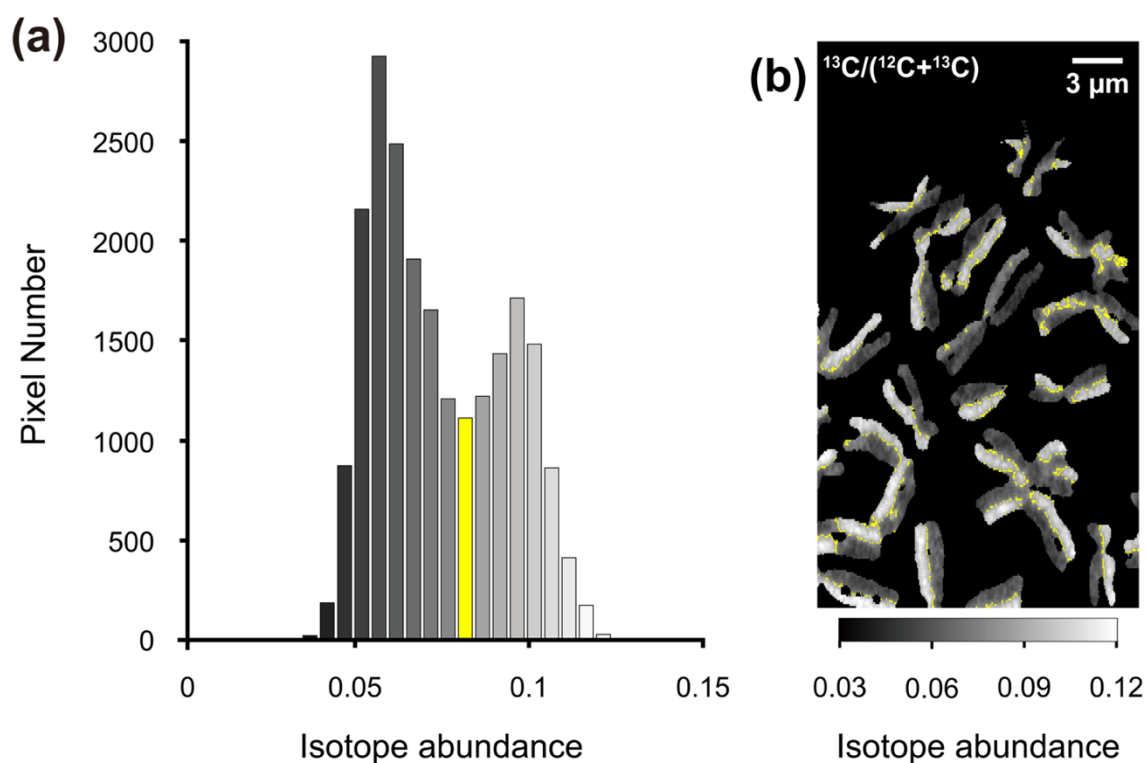
Figure 18: Corresponding position in isotope image for intermediate bin of peak B of Figure 21a. (a) The intermediate bin defined by yellow color. (b) Corresponding pixels of the yellow colored bin defined by yellow color.

3.3. RESULTS

The chromosome spread from single HeLa cell cultured with ^{13}C-labeled DMEM for 1 week showed uniform distribution of carbon isotope abundance (Figure 19). Individual chromosomes cultured with replaced medium (DMEM and BrdU with natural carbon isotope abundance) for 32h showed uniform distributions of total carbon but, in the case of carbon isotope abundance consisted of pair of ^{13}C-rich region and ^{13}C-poor region which directly adjusted each other

(Figure 20b). The pair texture suggests that the ^{13}C-rich and ^{13}C-poor regions correspond to a sister chromatid pair of a HeLa cell chromosome. Then exchanges between the sister chromatids were observed in some chromosomes. The sister chromatid pair also showed rich and poor regions for Br. The differences of ^{13}C and Br intensities were observed in all pairs of sister chromatid.

Figure 19: Carbon isotope abundance image of a chromosome spread from single HeLa cell incubated with stable isotope labeled medium for 1 week.
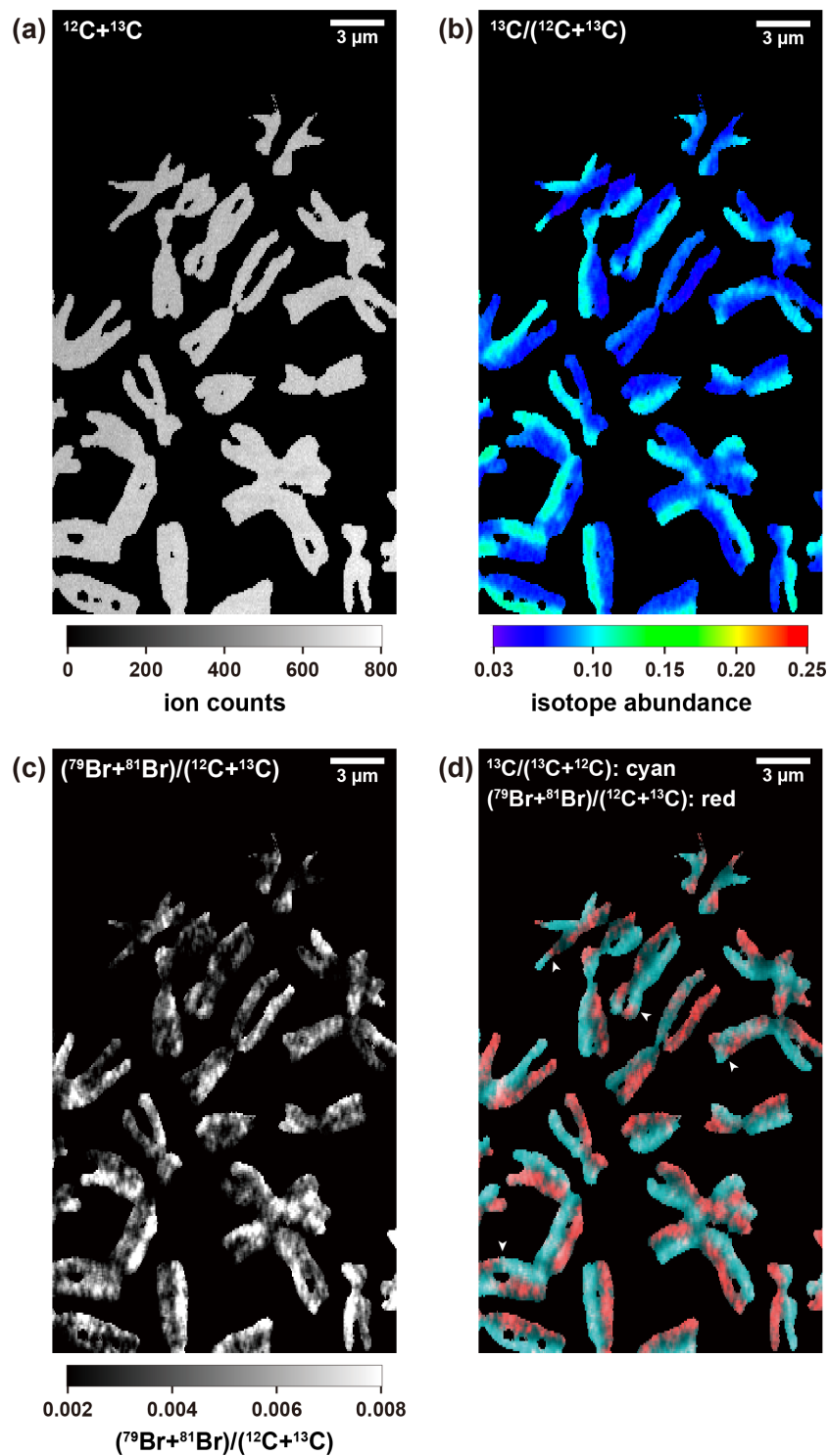
Figure 20: Images of a chromosome spread from single HeLa cell incubated with DMEM administrated 15 µM BrdU for 32 h after 1 week stable isotope labeling. (a) $^{12}C + ^{13}C$.(b) Carbon isotope abundance. (c) $(^{79}Br + ^{81}Br)/(^{12}C + ^{13}C)$.(d) Merged image of (b) (cyan) and (c) (red).

The carbon isotope abundance displayed in Figures 19 and 20b appeared the same distributions as the chromosome replication model and reduced according to the successive cell cycles. Histograms of the carbon isotope abundance distributions were obtained from pixels inside the chromosomes and showed three peaks which correlate to the appearance of the chromosomes (Figure 21a). The carbon isotope abundance of the chromosomes from the ^{13}C-enriched cell showed one peak and 0.230 in average with standard deviation (SD) of 0.011 (peak A of Figure 21a). The carbon isotope abundance of the chromosomes from the cell cultured with replaced medium for 32 h showed two peaks which correspond to ^{13}C-rich and ^{13}C-poor chromatids. The ^{13}C-rich peak was 0.094 in average with SD of 0.010 (peak B_1 of Figure 21a). The ^{13}C-poor peak was 0.059 in average with SD of 0.010 (peak B_2 of Figure 21a). The carbon isotope abundances of the ^{13}C-poor chromatids were higher than the natural carbon isotope abundance (0.011).
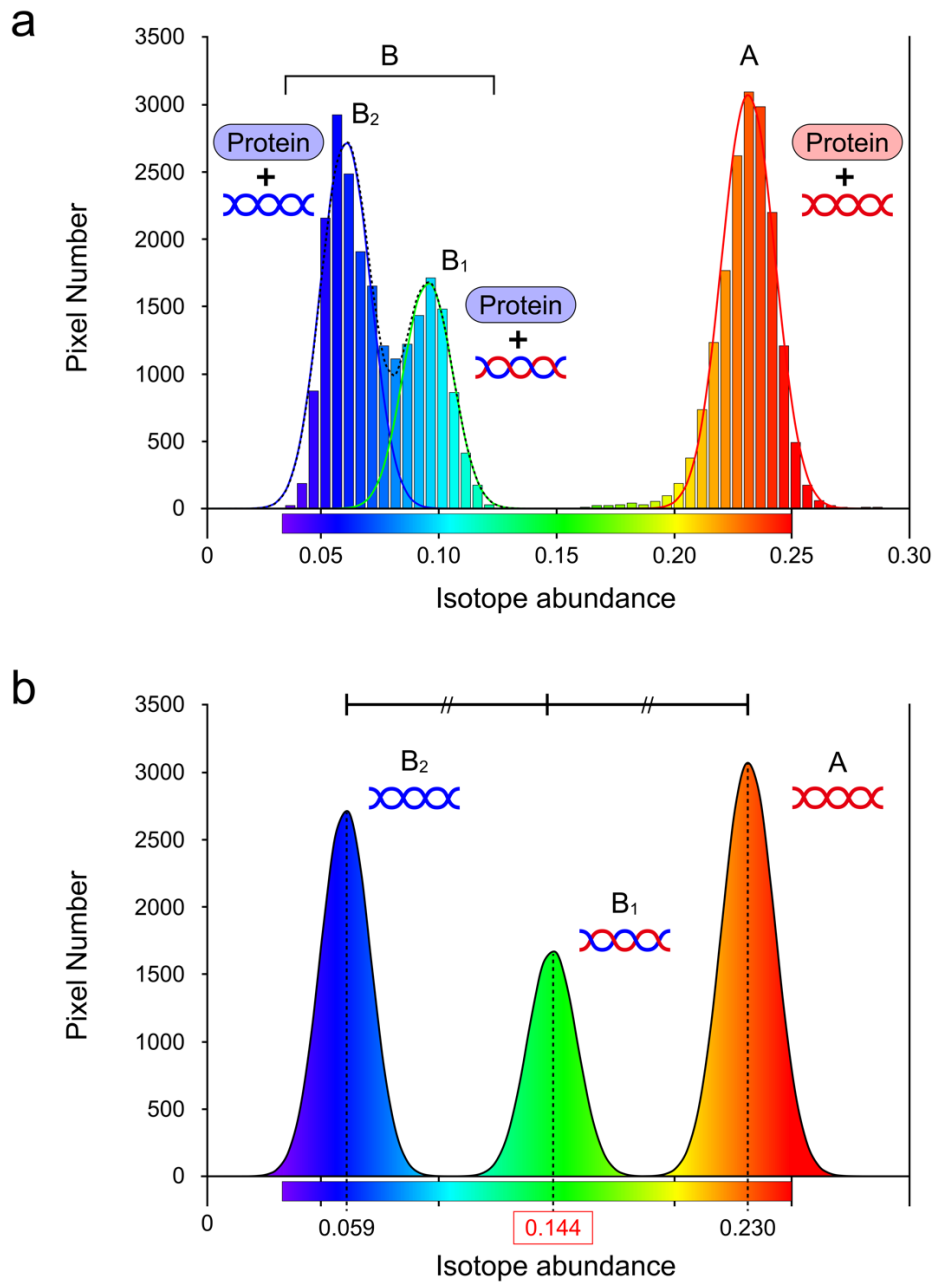
Figure 21: Histogram of carbon isotope abundance. (a) Chromosomes shown in Figure 19 and 20. (b) DNAs of Figure 21a. Peak B_1 shifts to the intermediate position between peaks A and B_2 after subtraction of contributions of histone components. Each peak was fitted by Gaussian curves (median ± standard deviation). A: Stable carbon isotope incubation for 1 week (0.230 ± 0.011). B: Natural carbon isotope incubation for 32 h after the stable carbon isotope incubation. The distribution is constructed by two Gaussian curves (B_1: 0.094 ± 0.010, B_2: 0.059 ± 0.010).

3.4. DISCUSSIONS

Br-rich regions displayed in Figure 20c indicate the distributions of the dsDNA labeled by BrdU which supplemented in replaced culture medium. Since the cells cultured with replaced medium for 32h contained Br-rich or Br-poor regions in all chromosomes, it is demonstrated that these cells entered second cell cycle (cycle-2) (Levi-Setti and Le Beau, 1992; Perry and Wolff, 1974). If the differences of ^{13}C intensity observed in cycle-2 chromosomes were caused by the existence of ^{13}C-rich ssDNA as illustrated in Figure 11, the Br-rich regions and the ^{13}C-rich regions should distribute complementarily in individual chromosomes. The merged image composed of Br and carbon isotope abundance showed the complementary distributions between Br-rich regions and ^{13}C-rich regions in all cycle-2 chromosomes (Figure 20d). Therefore we identified that the ^{13}C-rich regions in individual chromosomes correspond to the distributions of ^{13}C-rich ssDNA. This correspondence indicates that the reciprocal exchange of ^{13}C label observed in chromosomes shows the exchange of DNA strands and is sister chromatid exchange which was visualized by stable isotope labeling for the first time. These results indicate that the labeled DNA strand and the dynamics of individual chromosome segregations were traced in subcellular resolution by stable isotope imaging, and peaks A, B$_1$ and B$_2$ in Figure 21a corresponded to different labeling state of DNA of progressive cell division.

The HeLa cells cultured by U-^{13}C$_6$-Glucose for 1 week should have passed

10 cell cycles, since the cell used for this study divide every 16 h. Therefore, most cells are composed by the ^{13}C-labeled carbon from the culture medium. The carbon isotope abundance of the culture medium is calculated to be 0.238 from the chemical composition of the medium. The carbon isotope abundance in the chromosomes in the chromosomes just before medium replacement (0.230) corresponds to this calculation within standard deviation. The complementary distributions between Br-rich chromatids and ^{13}C-rich chromatids indicate that the ^{13}C-poor chromatids were composed by carbon from the culture medium with natural carbon isotope abundance. The ^{13}C-rich chromatids were composed of ssDNA synthesized from the U-^{13}C$_6$-Glucose containing medium and ssDNA and proteins synthesized from the culture medium with natural carbon isotope abundance. In order to synthesize the daughter cell components, supplies of nutrients from the culture medium with natural carbon isotope abundance was necessary. Therefore, at second cell cycle, the carbon isotope abundance of the initial DNA and proteins (0.230) are diluted fourfold with natural carbon isotope abundance (0.011) to 0.066. This value and the observed carbon isotope abundance of the ^{13}C-poor chromatids in the second cell cycle (0.059 ± 0.010) are in agreement within the error. The small deficit of the observed value may be due to some export of the original substrates, which may occur from the parent cell during cell divisions. Thus, the carbon isotope abundance of peak B$_2$ of Figure 21a shows that the chromatids (DNA and proteins) were synthesized during second cell cycle after the medium replacement.

The chromatids reflecting peak B_1 (0.094) mainly consist of DNA and histones. Several models have been proposed to explain the histone incorporations into chromatids through chromosome replications (Budhavarapu et al., 2013; English et al., 2017; Natsume et al., 2007; Xie et al., 2017). We hypothesized that the histones of peak B_1 were simultaneously synthesized with the histones composing peak B_2 in the second cell cycle, in which carbon isotope abundance was 0.059. The carbon amount ratios between DNA and histones composing peak B_1 could be calculated as follows. A nucleosome, the basic structural unit of a chromosome, consists of about 200 bp DNA and a pair of core histone and linker histone (Kornberg, 1974). In a human cell, the DNA consists of deoxyadenosine, thymidine, deoxycytidine and deoxyguanosine and contains 3918 carbon atoms per nucleosome (Lander et al., 2001). The core histone consists of 8 histone molecules (two molecules each of Histone H2A, H2B, H3, H4) and a linker histone consists of 1 histone molecule (Kornberg, 1974). Therefore, the histones per nucleosome contain 57740 carbon atoms, which are calculated from the protein sequences (ensemble ver. ENSG00000277075.2, ENSG00000180596.7, ENSG00000197153.4, ENSG00000158406.4, ENSG00000189060.5). As a result, the carbon amount ratio of DNA/histone of a chromosome is 0.41/0.59. If the carbon isotope abundance of the histones composing peak B_1 is calculated to be 0.144 (Figure 21b). The value corresponds to the middle of peak A and B_2. This correspondence demonstrates that the stable isotope labeling visualized the semi-conservative replication of individual DNA strands in a single cell quantitatively,

and suggests that the incorporation of histones occurred randomly through chromosome replication. The estimation of carbon isotope composition of histones in a chromosome may provide new approach to restrict nucleosome assembly mechanisms.

Figures 19 and 20b show the increase of carbon isotope abundance in HeLa cell DNA by using U-^{13}C$_6$-Glucose as stable isotope label. This is the result of that the cells synthesized base and/or deoxyribose using U-^{13}C$_6$-Glucose and incorporated into the DNA. Although the cells incorporate glucose mainly to use for energy source, parts of various intermediates provided from glucose degradation serve for the *de novo* synthesis of deoxyribonucleotides, which are structural unit of DNA (Alberts et al., 2013; Zhang et al., 2008). Among the substrates used for the carbon source of deoxyribonucleotide, ribose-5-phosphate (R5P) and aspartic acid are have to be synthesized from glucose, because DMEM do not contain them. R5P is synthesized from glucose-6-phosphate, which is the intermediate in glycolysis, via the pentose phosphate pathway. Aspartic acid is synthesized from oxaloacetic acid, which is the intermediate in tricarboxylic acid (TCA) cycle, by receiving an amino group from glutamic acid (Figure 22). The incorporation of 4 types of deoxyribonucleotides derived from U-^{13}C$_6$-Glucose can result in labeling over half of carbon atoms constructing DNA. Thus, DNA labeling procedure using labeled glucose is expected to increase labels in the whole of DNA compared to labeled thymidine. The stable isotope imaging technique described here has analytical limitations for scanning. The pulsed primary ion

beam for time-of-flight mass spectrometry prolongs the scanning time and sets the spatiotemporal restriction on imaging. However, shorten imaging should be possible by development of analysis software for optimal selection of region of interest. On the other hand, this approach for imaging the distributions of stable isotopes has some advantages over previously available methods. Labeling of ^{3}H-dT and BrdU induces congenital malformations, lengthened cell cycles, DNA fragmentation, premature senescence and cell death (Bannigan and Langman, 1979; Lehner et al., 2011; Ross et al., 2008; Solary et al., 1992). In contrast, the combination technique in this study can avoid the cytotoxicity caused by label incorporations into the cells and enable to analyze cytogenetic alterations without these effects. The safe properties of this technique make it possible to apply the long term tracking over multiple round of cell cycles.
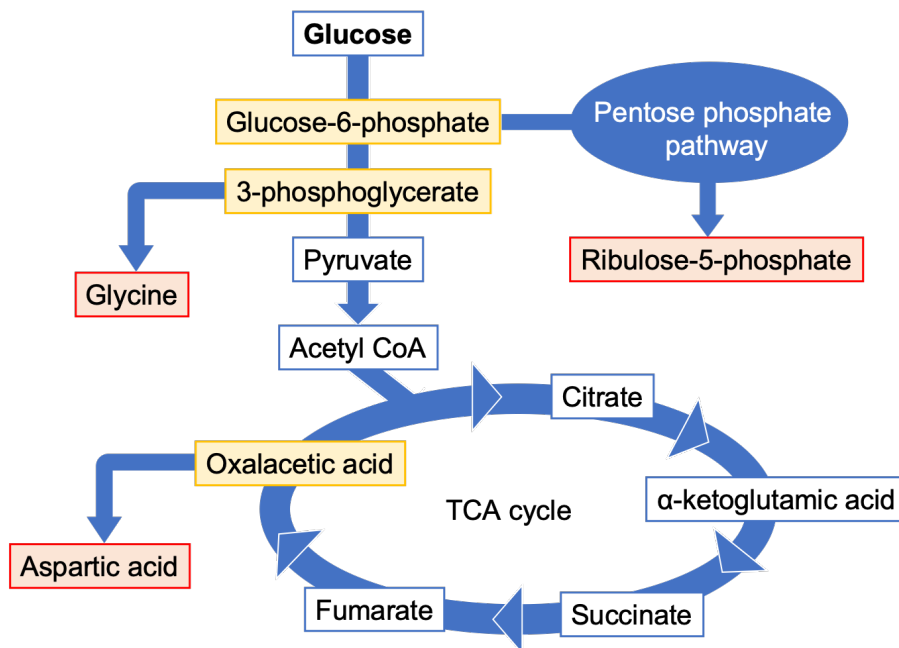
Figure 22: Schematic of a part of glucose metabolic pathway. The intermediates of glucose metabolic pathway produce ribulose-5-phosphate, aspartic acid and glycine that are used as the carbon source for deoxyribonucleotides.

3.6. SUMAMRY

We studied stable isotope-labeled chromosomes of the human cultured cell by stable isotope imaging. The ion images show distinctive carbon isotope abundances of chromatids corresponding to each cell division step demonstrating semi-conservative DNA replication for individual chromosomes. The images also detected sister chromatid exchanges. Non-analog imaging of chromatids allows to evaluate the spontaneous genome instabilities without mutagens. The combination of stable isotope labeling and nano-scale isotope imaging may be a new unique powerful approach for studies on biological systems in cells in addition to conventional techniques using radioisotopes, chemical analogs and fluorescent tags.

4. CONCLUSIONS

The high lateral resolution and quantitative ion imaging technique was established to evaluate the traceability of the stable isotope labels incorporated into individual chromosomes. Firstly, the performance for ion imaging of isotope nanoscope equipping Ga liquid metal ion source and aberration corrector in the primary column was studied. Chromatic and spherical aberration correction with primary acceleration voltage of 20 kV made the diameter of primary ion beam 1.4 times smaller than the non-correction mode, therefore, the beam density at a given primary beam diameter became about two times larger with aberration correction mode than without aberration correction. Moreover, the lateral resolutions of ion images increased with the reduction of primary ion current and achieved to 20 nm at the primary ion current of 3 pA with acceleration voltage of 20 kV. High primary current density with lower acceleration voltage compared to conventional imaging mass spectrometer allows to obtain ion images of high lateral resolution with lower sample disruption.

Then, the distributions of stable isotope labels (^{13}C) incorporated into the chromosomes through the successive cell divisions were quantitated by using carbon isotope abundance images [$^{13}C/(^{12}C + {}^{13}C)$]. The differences in the label amounts among the sister chromatids resulted in the distributions of DNA strands labeled by U-$^{13}C_6$-Glucose and reflected the semi-conservative replication of DNA. The combination of stable isotope labeling and isotope nanoscope enables us to

trace the dynamics, segregation or inheritance of the organelles in the individual cells without radio isotopes and chemical tags. This methodology may be a unique and powerful tool to study cell biology in addition to conventional techniques.

ACKNOWLEDGEMENTS

REFERENCES

Alberts, B., Bray, D., Hopkin, K., Johnson, A., Lewis, J., Raff, M., Roberts, K., and Walter, P. (2013). Essential Cell Biology Fourth Edition (Garland Science).

Bajo, K., Olinger, C.T., Jurewicz, A.J.G., Burnett, D.S., Sakaguchi, I., Suzuki, T., Itose, S., Ishihara, M., Uchino, K., Wieler, R., et al. (2015). Depth profiling analysis of solar wind helium collected in diamond-like carbon film from Genesis. Geochem. J. *49*, 559–566.

Bajo, K., Itose, S., Matsuya, M., Ishihara, M., Uchino, K., Kudo, M., Sakaguchi, I., and Yurimoto, H. (2016). High spatial resolution imaging of helium isotope by TOF-SNMS. Surf. Interface Anal. *48*, 1190–1193.

Bannigan, J., and Langman, J. (1979). The cellular effect of 5-bromodeoxyuridine on the mammalian embryo. J. Embryol. Exp. Morphol. *VOL 50*, 123–135.

Bell, A.E. (1988). A low-current liquid metal ion source. J. Vac. Sci. Technol. B Microelectron. Nanom. Struct. *6*, 927.

Budhavarapu, V.N., Chavez, M., and Tyler, J.K. (2013). How is epigenetic information maintained through DNA replication? Epigenetics and Chromatin *6*, 1–7.

Dileep, V., and Gilbert, D.M. (2018). Single-cell replication profiling to measure stochastic variation in mammalian replication timing. Nat. Commun. *9*.

Ebata, S., Ishihara, M., Uchino, K., Itose, S., Matsuya, M., Kudo, M., Bajo, K., and Yurimoto, H. (2012). Development of laser ionization mass nanoscope

(LIMAS). Surf. Interface Anal. *44*, 635–640.

Ebata, S., Ishihara, M., Kumondai, K., Mibuka, R., Uchino, K., and Yurimoto, H. (2013). Development of an Ultra-High Performance Multi-Turn TOF-SIMS/SNMS System "MULTUM-SIMS/SNMS." Am. Soc. Mass Spectrom. *24*, 222–229.

English, C.M., Maluf, N.K., Tripet, B., Churchill, M.E.A., and Tyler, J.K. (2017). ASF1 Binds to a Heterodimer of Histones H3 and H4: A Two-Step Mechanism for the Assembly of the H3–H4 Heterotetramer on DNA. Biochemistry *176*, 139–148.

Gratzner, H.G., Leif, R.C., Ingram, D.J., and Castro, A. (1975). The use of antibody specific for bromodeoxyuridine for the immunofluorescent determination of DNA replication in single cells and chromosomes. Exp. Cell Res. *95*, 88–94.

Hamasaki, T., Matsumoto, T., Sakamoto, N., Shimahara, A., Kato, S., Yoshitake, A., Utsunomiya, A., Yurimoto, H., Gabazza, E.C., and Ohgi, T. (2013). Synthesis of 18O-labeled RNA for application to kinetic studies and imaging. Nucleic Acids Res. *41*.

Hervig, R.L., Mazdab, F.K., Williams, P., Guan, Y., Huss, G.R., and Leshin, L.A. (2006). Useful ion yields for Cameca IMS 3f and 6f SIMS: Limits on quantitative analysis. Chem. Geol. *227*, 83–99.

Hill, R. (1993). Using optimum magnification as a figure of merit to evaluate the performance of focused-ion-beam columns. In Charged-Particle Optics, p.

Ishihara, M., Ebata, S., Kumondai, K., Mibuka, R., Uchino, K., and Yurimoto, H. (2010). Ultra-high performance multi-turn TOF-SIMS system with a femto-

second laser for post-ionization : investigation of the performance in linear

mode †. *2010*, 1598–1602.

Ishitani, T., and Kawanami, Y. (1995). Coarse guidelines in designing focused

ion beam optics. J. Vac. Sci. Technol. B Microelectron. Nanom. Struct. *13*,

371.

Itose, S., Matsuya, M., Uno, S., Yamashita, K., Ebata, S., Ishihara, M., Uchino,

K., Yurimoto, H., Sakaguchi, K., and Kudo, M. (2011). An Aberration

Corrected FIB for Nano-Area Mass Spectrometry. Microsc. Microanal. *17*,

654–655.

Kornberg, R.D. (1974). Chromatin Structure : A Repeating Unit of Histones and

DNA. Science *184*, 868–871.

Kruit, P., and Jiang, X.R. (1996). Influence of Coulomb interactions on choice of

magnification, aperture size, and source brightness in a two lens focused

ion beam column. J. Vac. Sci. Technol. B Microelectron. Nanom. Struct.

Kuga, Y., Sakamoto, N., and Yurimoto, H. (2014). Stable isotope cellular

imaging reveals that both live and degenerating fungal pelotons transfer

carbon and nitrogen to orchid protocorms. New Phytol. Trust *202*, 594–605.

Lander, E.S., Linton, L.M., Birren, B., Nusbaum, C., Zody, M.C., Baldwin, J.,

Devon, K., Dewar, K., Doyle, M., Fitzhugh, W., et al. (2001). Initial

sequencing and analysis of the human genome: International Human

Genome Sequencing Consortium. Nature *412*, 565–566.

Latt, S.A. (1973). Microfluorometric Detection of Deoxyribonucleic Acid

Replication in Human Metaphase Chromosomes. Proc. Natl. Acad. Sci. *70*,

3395–3399.

Lechene, C., Hillion, F., McMahon, G., Benson, D., Kleinfeld, A.M., Kampf, J.P., Distel, D., Luyten, Y., Bonventre, J., Hentschel, D., et al. (2006). High-resolution quantitative imaging of mammalian and bacterial cells using stable isotope mass spectrometry. J. Biol. *5*, 20.

Lehner, B., Sandner, B., Marschallinger, J., Lehner, C., Furtner, T., Couillard-Despres, S., Rivera, F.J., Brockhoff, G., Bauer, H.C., Weidner, N., et al. (2011). The dark side of BrdU in neural stem cell biology: Detrimental effects on cell cycle, differentiation and survival. Cell Tissue Res. *345*, 313–328.

Levi-Setti, R., and Le Beau, M. (1992). Cytogenetic applications of high resolution secondary ion imaging microanalysis: detection and mapping of tracer isotopes in human chromosomes. Biol. Cell *74*, 51–58.

Levi-Setti, R., and Timothy R. Fox (1980). High resolution scanning ion probes: Applications to physics and biology. Nucl. Instruments Methods *168*, 139–149.

Liu, H., Yan, P., and Fanning, E. (2015). Human DNA helicase B functions in cellular homologous recombination and stimulates rad51-mediated 5′ -3′ heteroduplex extension in vitro. PLoS One *10*, 1–17.

Malherbe, J., Penen, F., Isaure, M.P., Frank, J., Hause, G., Dobritzsch, D., Gontier, E., Horréard, F., Hillion, F., and Schaumlöffel, D. (2016). A New Radio Frequency Plasma Oxygen Primary Ion Source on Nano Secondary Ion Mass Spectrometry for Improved Lateral Resolution and Detection of Electropositive Elements at Single Cell Level. Anal. Chem. *88*, 7130–7136.

Meselson, M., and Stahl, F.W. (1958). The replication of DNA in Escherichia

coli. Proc. Natl. Acad. Sci. *44*, 671–682.

Mibuka, R., Hassaballa, S., Uchino, K., Yurimoto, H., Todokoro, R., Kumondai, K., and Ishihara, M. (2008). Characteristics of post-ionization using a femto-second laser. Appl. Surf. Sci. *255*, 1595–1598.

Migeon, H.N., Saldi, F., Gao, Y., and Schuhmacher, M. (1995). Ion microscope and ion microprobe analysis under oxygen, cesium and gallium bombardment. Int. J. Mass Spectrom. Ion Process. *143*, 51–63.

Nagata, K., Bajo, K., Itose, S., Matsuya, M., Ishihara, M., Uchino, K., and Yurimoto, H. (2019). Aberration-corrected focused ion beam for time-of-flight secondary neutral mass spectrometry_supplementary data. Appl. Phys. Express 15–18.

Natsume, R., Eitoku, M., Akai, Y., Sano, N., Horikoshi, M., and Senda, T. (2007). Structure and function of the histone chaperone CIA/ASF1 complexed with histones H3 and H4. Nature *446*, 338–341.

Orloff, J. (1987). Comparison of optical design approaches for use with liquid metal ion sources. J. Vac. Sci. Technol. B Microelectron. Nanom. Struct.

Perry, P., and Wolff, S. (1974). New Giemsa method for the differential staining of sister chromatids. Nature *251*, 156–158.

Pinkel, D., Thompson, L.H., Gray, J.W., and Vanderiaan, M. (1985). Measurement of Sister Chromatid Exchanges at Very Low Bromodeoxyuridine Substitution Levels Using a Monoclonal Antibody in Chinese Hamster Ovary Cells. Cancer Res. *45*, 5795–5798.

Ross, H.H., Levkoff, L.H., Marshall, G.P., Caldeira, M., Steindler, D.A., Reynolds, B.A., and Laywell, E.D. (2008). Bromodeoxyuridine Induces

Senescence in Neural Stem and Progenitor Cells. Stem Cells *26*, 3218–
3227.

Sakaguchi, K., and Sekine, T. (1998). Focused ion beam optical column design
and consideration on minimum attainable beam size. J. Vac. Sci. Technol.
B Microelectron. Nanom. Struct. *16*, 2462.

Sakamoto, T., Koizumi, M., Kawasaki, J., and Yamaguchi, J. (2008).
Development of a high lateral resolution TOF-SIMS apparatus for single
particle analysis. *255*, 1617–1620.

Solary, E., Bertrand, R., Jenkins, J., and Pommier, Y. (1992). Radiolabeling of
DNA can induce its fragmentation in HL-60 human promyelocytic
leukemic cells. Exp. Cell Res. *203*, 495–498.

Steinhauser, M.L., Bailey, A.P., Senyo, S.E., Guillermier, C., Perlstein, T.S.,
Gould, A.P., Lee, R.T., and Lechene, C.P. (2012). Multi-isotope imaging
mass spectrometry quantifies stem cell division and metabolism. Nature
481, 516–519.

Swanson, L.W., Schwind, G.A., Bell, A.E., and Brady, J.E. (1979). Emission
characteristics of gallium and bismuth liquid metal field ion sources. J. Vac.
Sci. Technol. *16*, 1864–1867.

Takahashi, S., Miura, H., Shibata, T., Nagao, K., Okumura, K., Ogata, M.,
Obuse, C., Takebayashi, S. ichiro, and Hiratani, I. (2019). Genome-wide
stability of the DNA replication program in single mammalian cells. Nat.
Genet. *51*, 529–540.

Taupin, P. (2007). BrdU immunohistochemistry for studying adult neurogenesis:
Paradigms, pitfalls, limitations, and validation. Brain Res. Rev. *53*, 198–

214.

Taylor, J.H., Woods, P.S., and Hughes, W.L. (1957). The Organization and Duplication of Chromosomes As Revealed By Autoradiographic Studies Using Tritium-Labeled Thymidinee. Proc. Natl. Acad. Sci. *43*, 122–128.

Tonotani, A., Bajo, K., Itose, S., Ishihara, M., Uchino, K., and Yurimoto, H. (2016). Evaluation of multi-turn time-of-flight mass spectrum of laser ionization mass nanoscope. Surf. Interface Anal. *48*, 1122–1126.

Wang, L. (1997). Design optimization for two lens focused ion beam columns. J. Vac. Sci. Technol. B Microelectron. Nanom. Struct. *15*, 833.

Watson, J., and Crick, F. (1953). Genetical implications of the structure of deoxyribonucleic acid. Nature *171*, 964–967.

Weißbäcker, C. (2001). Dissertation T U Darmstadt.

Weißbäcker, C., and Rose, H. (1999). Optik 110, Suppl. 8, 0106, 8.

Weißbäcker, C., and Rose, H. (2000). Proc 12th European Congress On Electron Microscopy, Brno, Vol.3. 157–158.

Weißbäcker, C., and Rose, H. (2001). Electrostatic correction of the chromatic and of the spherical aberration of charged-particle lenses (Part I). J. Electron Microsc. (Tokyo). *50*, 383–390.

Weißbäcker, C., and Rose, H. (2002). Electrostatic correction of the chromatic and of the spherical aberration of charged-particle lenses (Part II). J. Electron Microsc. (Tokyo). *51*, 45–51.

Xie, J., Wooten, M., Tran, V., and Chen, X. (2017). Breaking Symmetry − Asymmetric Histone Inheritance in Stem Cells. Trends Cell Biol. *27*, 527–540.

Yurimoto, H., Bajo, K., Sakaguchi, I., Suzuki, T.T., Jurewicz, A.J.G., Itose, S., Uchino, K., and Ishihara, M. (2016). Quantitative analysis of helium by post-ionization method using femtosecond laser technique. Surf. Interface Anal. *48*, 1181–1184.

Zach, J. (2006). 16th Int. Microsc. Congr., 2006 (Sapporo) Vol. 2. 662.

Zhang, Y., Morar, M., and Ealick, S.E. (2008). Structural biology of the purine biosynthetic pathway. Cell. Mol. Life Sci. *65*, 3699–3724.